Confining Light to Deep Subwavelength Dimensions to Enable Optical Nanopatterning

Trisha L. Andrew, *et al.*

Science **324**, 917 (2009);
DOI: 10.1126/science.1167704

tion times was performed by using a photomask lithographic approach as shown in Fig. 3C, where resin on a transparent substrate is irradiated uniformly through the substrate with the initiating wavelength while being irradiated by the inhibiting wavelength through a photomask. As a result, the masked region polymerizes and becomes insoluble, whereas the unmasked region remains liquid and is readily washed away.

The fabrication of complex, 3D microstructures requires that the doughnut of inhibiting radicals created spatially to refine the polymerization region be translated in conjunction with the writing spot without leaving a termination trail. This desired behavior in turn requires that the inhibiting species are rapidly eliminated in the absence of the photoinhibition irradiation wavelength. The rapid cessation of photoinhibition in the current system is demonstrated in Fig. 3D. During UV irradiation periods, the polymerization slowed dramatically, as evidenced by the reduced rate of increase in the storage and loss moduli; however, when the UV irradiation ceased, the polymerization rate underwent an immediate and marked increase.

To demonstrate that this polymerization rate control is useful to initiate polymerization below the optical diffraction limit, as predicted by Fig. 1D, we implemented the direct-write lithography scheme shown in Fig. 1A. Polymer voxels were created on a glass substrate and imaged by scanning electron microscopy (SEM) after solvent wash, as shown in Fig. 4A. As predicted in Fig. 1D, increasing the UV power, and therefore the photoinhibition rate, of the GL mode progressively reduces the voxel diameter in a controllable manner. In the sequence shown, the constant-power, 1.3-μm (full width to $1/e^2$) blue focus has written polymer voxels with diameter varying from 3.6 μm with no UV down to 200 nm for strong UV inhibition at 100 μW UV irradiation power. This resolution is typical of two-photon initiation using ~1.4 numerical aperture (NA) lenses (*2*, *5*) with aberration-limited depth ranges of tens of μm; the much lower NA demonstrated here enables mm-scale thicknesses. In Fig. 4B we show the ability to create 110-nm voxels full width and 65 nm full width at half maximum by using a 1.3-NA lens and measured by SEM, approaching the size of the smallest features produced with use of two-photon photopolymerization (*6*). Continuous writing under these conditions with the superimposed Gaussian/GL irradiation scheme is shown in Fig. 4C, resulting in lines of similar diameter. Reduction of voxel diameters using this irradiation scheme could be effected in other materials such as those containing reversibly photodimerizable functionalities, where dimers are created by irradiation at one wavelength and cleaved by irradiation at a different wavelength; however, photoreversibility precludes translation of a writing spot and disallows fabrication of dense, 3D structures.

Two-photon photopolymerization has been described as the only microprocessing approach with intrinsic 3D fabrication capability (*18*). Although the optical approach demonstrated here produces confinement of the polymerized region along only two axes, manipulation of the photoinhibiting wavelength into a bottle beam profile (*19*) would induce confinement along the third axis, thus allowing fabrication of 3D structures with sub–100-nm isotropic resolution. Because single-photon absorption cross sections are often orders of magnitude larger than two-photon cross sections, this photoinitiation-photoinhibition system facilitates the use of inexpensive continuous wave (CW) diode lasers and very high write velocities. Thus, this single-photon approach to nanolithography uses dramatically cheaper hardware and scales to much higher throughput.

References and Notes

1. A. C. Sullivan, M. W. Grabowski, R. R. McLeod, *Appl. Opt.* **46**, 295 (2007).
2. S. Kawata, H.-B. Sun, T. Tanaka, K. Takada, *Nature* **412**, 697 (2001).
3. B. H. Cumpston *et al.*, *Nature* **398**, 51 (1999).
4. H.-B. Sun *et al.*, *Opt. Lett.* **25**, 1110 (2000).
5. T. Tanaka, H.-B. Sun, S. Kawata, *Appl. Phys. Lett.* **80**, 312 (2002).
6. W. Haske *et al.*, *Opt. Express* **15**, 3426 (2007).
7. N. C. Strandwitz *et al.*, *J. Am. Chem. Soc.* **130**, 8280 (2008).
8. K. Ichimura, M. Sakuragi, *J. Polym. Sci. Polym. Lett. Ed.* **26**, 185 (1988).
9. S.-K. Lee, D. C. Neckers, *Chem. Mater.* **3**, 852 (1991).
10. S.-K. Lee, D. C. Neckers, *Chem. Mater.* **3**, 858 (1991).
11. D. J. Lougnot, D. Ritzenthaler, C. Carre, J. P. Fouassier, *J. Appl. Phys.* **63**, 4841 (1988).
12. S. K. Soh, D. C. Sundberg, *J. Polym. Sci. Polym. Chem. Ed.* **20**, 1299 (1982).
13. G. Donnert *et al.*, *Proc. Natl. Acad. Sci. U.S.A.* **103**, 11440 (2006).
14. Materials and methods and a study examining the effect of exposure time on polymerized feature size are detailed in supporting material available on *Science* Online.
15. P. J. Flory, in *Principles of Polymer Chemistry* (Cornell Univ. Press, Ithaca, NY, 1953).
16. L. G. Lovell, B. J. Elliott, J. R. Brown, C. N. Bowman, *Polymer* **42**, 421 (2001).
17. F. Chambon, H. H. Winter, *J. Rheol.* **31**, 683 (1987).
18. H. B. Sun, S. Kawata, in *NMR - 3D Analysis - Photopolymerization* (Springer, Berlin, 2004), vol. 170, pp. 169–273.
19. J. Arlt, M. J. Padgett, *Opt. Lett.* **25**, 191 (2000).

20. Supported by NSF programs IIP-0750506, IIP-0822695, and ECS-0636650, NIH grant DE10959, and the University of Colorado Innovative Seed Grant Program. A preliminary patent based on this technology has been filed by T.F.S., A.C.S., C.N.B., and R.R.M.

Supporting Online Material

www.sciencemag.org/cgi/content/full/1167610/DC1
Materials and Methods
Fig. S1
References

23 October 2008; accepted 24 March 2009
Published online 9 April 2009;
10.1126/science.1167610
Include this information when citing this paper.

Confining Light to Deep Subwavelength Dimensions to Enable Optical Nanopatterning

Trisha L. Andrew,[1] Hsin-Yu Tsai,[2,3] Rajesh Menon[3,4]*

In the past, the formation of microscale patterns in the far field by light has been diffractively limited in resolution to roughly half the wavelength of the radiation used. Here, we demonstrate lines with an average width of 36 nanometers (nm), about one-tenth the illuminating wavelength λ_1 = 325 nm, made by applying a film of thermally stable photochromic molecules above the photoresist. Simultaneous irradiation of a second wavelength, λ_2 = 633 nm, renders the film opaque to the writing beam except at nodal sites, which let through a spatially constrained segment of incident λ_1 light, allowing subdiffractional patterning. The same experiment also demonstrates a patterning of periodic lines whose widths are about one-tenth their period, which is far smaller than what has been thought to be lithographically possible.

Optical patterning is the primary enabler of microscale devices. However, the Achilles heel of optics is resolution. The far-field diffraction barrier limits the resolution of optical systems to approximately half the wavelength (*1*) and therefore restricts nanoscale patterning at visible wavelengths. Scanning electron beam patterning has thus become the preferred method for fabricating nanostructures. However, electrons are affected by extraneous electromagnetic fields, limiting the accuracy with which patterns can be placed relative to one another (*2*). Furthermore, electron flux is limited by mutual repulsion effects, constraining the patterning speed (*3*). The vacuum environment and electron lenses increase system complexity and cost. Alternatively, the diffraction barrier can be overcome in the optical

[1]Department of Chemistry, Massachusetts Institute of Technology (MIT), Cambridge, MA 02139, USA. [2]Department of Electrical Engineering and Computer Science, MIT, Cambridge, MA 02139, USA. [3]Research Laboratory of Electronics, MIT, Cambridge, MA 02139, USA. [4]LumArray, Somerville, MA 02143, USA.

*To whom correspondence should be addressed. E-mail: rmenon@mit.edu

near field (*4*). The high spatial frequencies present in the optical near field are evanescent, and hence the recording medium needs to be placed at a precisely controlled nanometric distance from the source of the optical near field (*5*–*7*). By placing a prepatterned photomask in intimate contact with the photoresist, the optical near field may be recorded (*8*). In this case, high resolution is achieved at the expense of an inflexible and costly photomask and the high probability of contamination of the contacted surfaces. An alternative approach scans one or many nanoscale tips in close proximity to the sample (*9*). Precisely maintaining the gap between the tip (or tips) and the sample is problematic, especially when patterning over large areas or with multiple near-field probes (*10*). Plasmonic lenses can alleviate some of these problems (*11*), but they still require gaps of <100 nm and nanometric gap control (*12*, *13*).

To overcome these limitations, we used a thin photochromic film on top of the recording photoresist layer. The molecules chosen to comprise the film adopt two isomeric forms that interconvert on respective absorptions of light at ultraviolet (λ_1) and visible (λ_2) wavelengths (*14*). We simultaneously applied both colors in an interference pattern that overlaps peaks at λ_1 with nodes at λ_2. Absorption at λ_1 generates the isomer transparent at that wavelength, but regions exposed to λ_2 revert to the initial isomer and continue to absorb at λ_1, protecting the photoresist. Only at the λ_2 nodes does a stable transparent aperture form (Fig. 1A) (*15*). Photons at λ_1 penetrate this aperture, forming a nanoscale writing beam that can pattern the underlying photoresist. The size of the aperture decreases as the ratio of the intensity at λ_2 with respect to that at λ_1 increases (*15*, *16*). This technique, which we refer to as absorbance modulation, can therefore confine light to spatial dimensions far smaller than the wavelength.

Furthermore, because the photochromic molecules recover their initial opaque state, spatial periods smaller than the incident wavelengths can be achieved by repeated patterning (*17*). In Fig. 1B, we plot the simulated full width at half maximum (FWHM) of the transmitted light at λ_1 as a function of the ratio of intensities at the two wavelengths, illustrating that the transmitted light is spatially confined to dimensions far below the wavelength. In other words, optical near fields are generated without bringing a physical probe into close proximity with the sample. In the past, we used an interferometric setup to illuminate an azobenzene polymer–based photochromic film with a standing wave at λ_2 and uniform illumination at λ_1 (*16*). Although linewidths as small as $\lambda_1/4$ were demonstrated, the thermal instability of the azobenzene polymer as well as the nonnegligible sensitivity of the underlying photoresist to λ_2 prevented further scaling below 100 nm.

For optimum performance, it is essential that the photochromic molecules are thermally stable; otherwise, the size of the writing beam becomes dependent on the absolute intensities rather than their ratio alone. If the photochromic molecule in the transparent state is thermally unstable, then at low-λ_1 intensities the thermal back-reaction overwhelms the forward (opaque-to-transparent) reaction, essentially closing the aperture. The FWHM of the resulting beam shows a minimum. This is illustrated in Fig. 1B, in which the photochromic parameters of 1,2-bis(5,5′-dimethyl-2,2’-bithiophen-yl) perfluorocyclopent-1-ene (compound **1**) (Fig. 1C) were assumed (*18*). A thermal rate constant of 5×10^{-4} s^{-1} was assumed for the dashed curve. The incident illumination is modeled as standing waves with a period of 350 nm (λ_2 = 633 nm) and 170 nm (λ_1 = 325 nm). Both curves were calculated by decreasing the peak

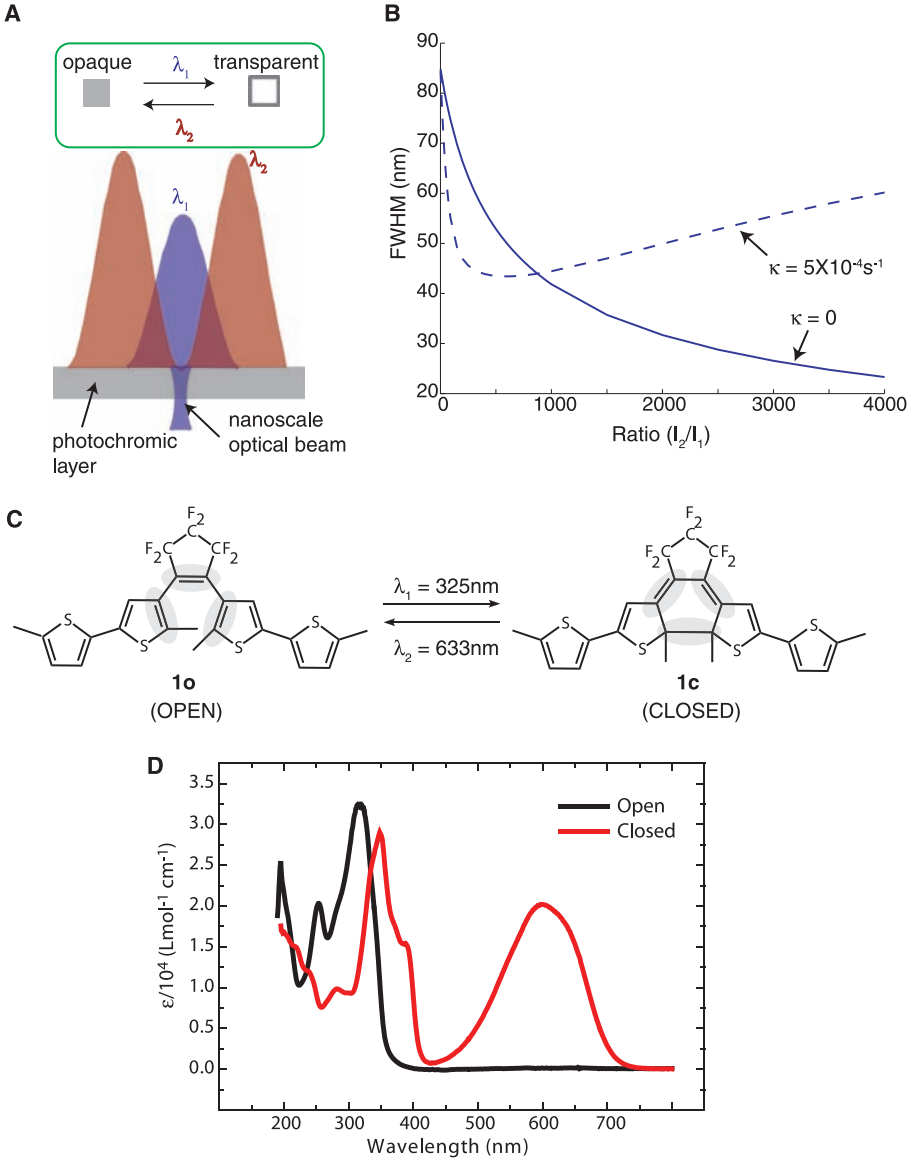

Fig. 1. The scheme of absorbance modulation. (**A**) The photochromic layer turns transparent upon exposure to λ_1 and opaque upon exposure to λ_2. When illuminated with a node at λ_2 coincident with a peak at λ_1, a subwavelength transparent region (or aperture) is formed through which photons at λ_1 penetrate, forming a nanoscale optical writing beam. (**B**) FWHM of the intensity distribution at λ_1 directly beneath the photochromic layer as a function of the ratio of the peak intensities at the two wavelengths. When the photochromic molecules are thermally stable [the thermal rate constant (κ) = 0], the size of the writing beam decreases monotonically, far below the wavelength. However, when a thermal instability is present ($\kappa = 5 \times 10^{-4}$ s^{-1}), the smallest beam size is limited, as shown by the dashed line. (**C**) Structures of the open- and closed-ring isomers of compound **1**. (**D**) Absorbance spectra of compound **1** in the open and closed forms in hexane. ε is the decadic molar absorptivity.

intensity of the λ_1 standing wave while maintaining the peak intensity of the λ_2 standing wave equal to 1 kW m^{-2} and repeating the numerical simulation for each intensity ratio. Although this deleterious effect can be overcome by using higher intensities at both wavelengths while maintaining the required intensity ratio, it is highly desirable to achieve nanoscale resolution at low intensities. For this reason, we turned our attention to thermally stable classes of photochromes, such as fulgides (*19*) and diarylethenes (*20*). In both of these classes of photochromes, photoinduced electrocyclic rearrangements transform a colorless (UV-absorbing) triene system into a highly colored cyclohexadiene photoproduct and vice versa. Because covalent bonds are either formed or broken during the photoisomerization process, conversion between the open-ring and closed-ring isomers is primarily photoinitiated, and the thermal contribution to this isomerization is negligible.

Initial investigations of furyl fulgide (*21*) as the active component in the absorbance-modulation layer (AML) revealed a susceptibility to photodegradation that significantly reduced the concentration of this photochrome in the AML with prolonged irradiation. Cursory analysis of some fulgides reported in the chemical literature confirmed that many fulgides display a lack of fatigue resistance because of photooxidation of either their triene or heterocyclic moieties (*19*). Therefore, we explored a comparatively photostable class of thiophene-substituted fluorinated cyclopentenes as potential photochromes for absorbance modulation. The perfluorinated bridge in these systems prevents photooxidation of the active triene moiety and suppresses competing nonproductive isomerization pathways. Specifically, compound **1** (Fig. 1C) was chosen for use in the AML because it displayed an absorption band centered at 313 nm in the open state and one centered at 582 nm in the closed state (Fig. 1D). These spectral features allowed the use of the 325-nm line of the helium-cadmium laser and the 633-nm line of the helium-neon laser for the writing and the confining beams, respectively. High intensities could be applied at the nodal wavelength λ_2 because 633-nm light has no effect on most photoresists.

Pertinent photophysical constants, such as absorption coefficients and photoreaction quantum yields, were measured for compound **1** at room temperature in hexane solution [table S1 and supporting online material (SOM) text].

In order to spin-cast the photochromic layer, we used a 30 mg ml^{-1} solution of poly(methyl methacrylate) (PMMA) in anisole doped with 92 weight percent compound **1** (with respect to PMMA) (*20*). The photochromic layer was to be placed atop a photoresist layer in order to record the transmitted light at λ_1. The solvent for the PMMA matrix, anisole, distorts the development rate of the photoresist. Therefore, a barrier layer of polyvinyl alcohol (PVA) was placed in between the two layers. The barrier layer also prevents any interdiffusion between the two layers. Because the high–spatial frequency content of the nanoscale writing beam is evanescent, it is important to keep the thickness of the PVA layer as small as possible.

In order to illustrate the effect of the thickness of the PVA layer on the linewidth of the pattern, we simulated the transmission of light through a subwavelength aperture in a metal

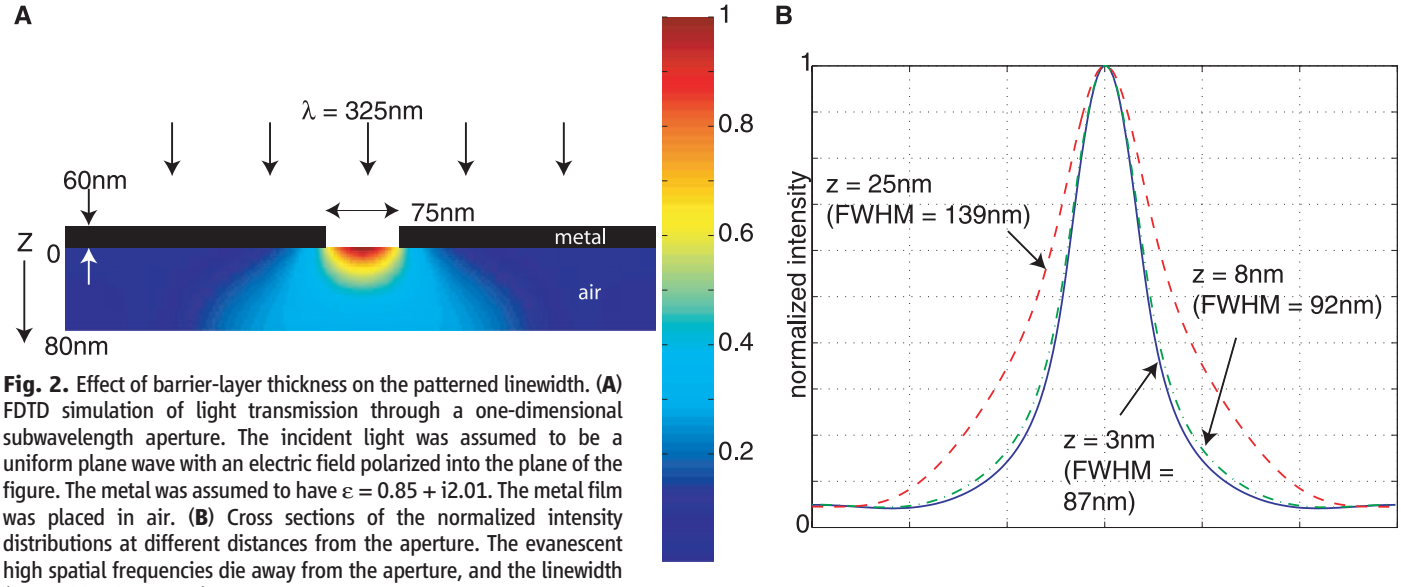

Fig. 2. Effect of barrier-layer thickness on the patterned linewidth. (**A**) FDTD simulation of light transmission through a one-dimensional subwavelength aperture. The incident light was assumed to be a uniform plane wave with an electric field polarized into the plane of the figure. The metal was assumed to have $\varepsilon = 0.85 + i2.01$. The metal film was placed in air. (**B**) Cross sections of the normalized intensity distributions at different distances from the aperture. The evanescent high spatial frequencies die away from the aperture, and the linewidth (defined by the FWHM) increases.

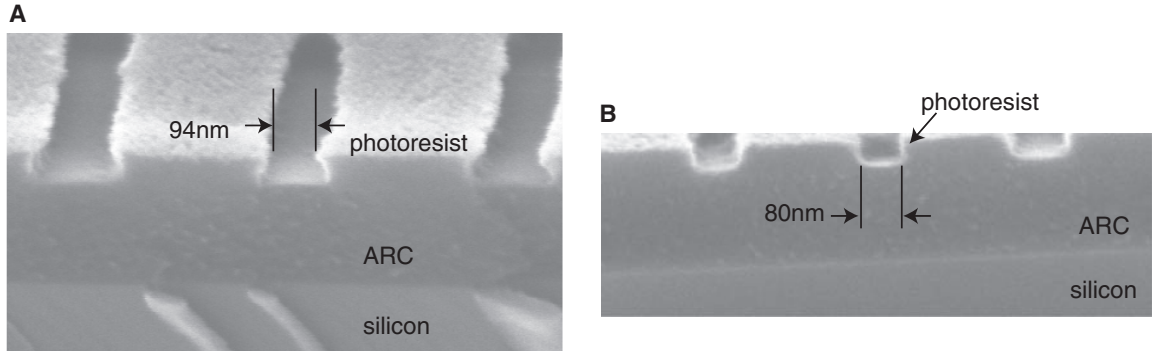

Fig. 3. Scanning electron micrographs of cross sections of exposed and developed lines in photoresist in which the PVA barrier layer thickness was (**A**) 25 nm and (**B**) 8 nm, respectively. The thinner the PVA layer is, the straighter is the resist sidewall and smaller is the exposed line. In both cases, the period of the lines is 350 nm, corresponding to the period of the λ_2 standing wave.

film using custom software that implements the finite-difference time-domain (FDTD) method (*22*). When a subwavelength aperture is illuminated, the transmitted light is primarily composed of evanescent high–spatial frequency components. These components decay exponentially away from the aperture, increasing the FWHM of the transmitted light. The illumination of a one-dimensional aperture with a width of 75 nm was simulated with a plane wave with a wavelength of 325 nm, as shown in the schematic in Fig. 2A. The electric field of the incident wave was polarized normal to the plane of the figure. The time-averaged intensity of the scattered light was calculated at steady state. Cross sections of the normalized intensity distribution in planes parallel to the aperture at varying distances from the aperture were computed and plotted in Fig. 2B. Clearly, the transmitted light is substantially broadened with distance from the aperture. Furthermore, the peak intensity at the center of the line also falls exponentially with distance from the aperture.

These theoretical predictions were qualitatively confirmed by our experimental results. Figure 3, A and B, shows scanning electron micrographs of the cross sections of exposed and developed photoresist with PVA barrier layer thicknesses of 25 nm and 8 nm, respectively. With the 25 nm layer, the exposed line exhibits considerable broadening with depth into the photoresist. The sidewall profile bears a qualitative resemblance to the intensity contours in Fig. 2A. With the thinner PVA, this linewidth broadening is noticeably curtailed, and the photoresist exhibits vertical sidewalls. This result also suggests that an ultrathin photoresist layer may be necessary to faithfully record the high spatial frequencies in the near field, which is in agreement with earlier work (*23*).

To minimize this effect of line broadening, we used a PVA film thickness of 8 nm, which was found to be sufficient to protect the photoresist from the solvent for the photochromic layer. Samples consisted of a silicon substrate spin-coated with 200 nm of anti-reflection coating, 200 nm of photoresist, 8 nm of PVA, and 410 nm of the photochromic layer. After exposure, the samples were rinsed in de-ionized water in a sonicator for about 5 min, which removed the PVA layer as well as the photochromic overlayer. The photoresist was baked on a hotplate at 120°C for 90 s and developed in 0.26 N tetramethyl ammonium hydroxide for 60 s. The resulting patterns were inspected in a scanning electron microscope after sputter-coating them with ~2 nm of a palladium/gold alloy.

The exposure system was a modified Lloyd's-mirror interferometer (fig. S5), consisting of a mirror at right angles to a vacuum chuck that held the sample. This configuration was illuminated at λ_1 = 325 nm and λ_2 = 633 nm. The angles of incidence of the two wavelengths were adjusted so that the resulting standing waves on the sample had periods of 350 nm at λ_2 = 633 nm and 170 nm at λ_1 = 325 nm (*18*). As illustrated in Fig. 4A, the nodes of the λ_2 standing wave approximately coincide with every other peak of the λ_1 standing wave. Photokinetic simulation using the extracted photochromic parameters reveal that the transmitted light at λ_1 is substantially narrower than the diffraction limit. The scanning electron micrograph in Fig. 4B shows that the average width of the lines recorded in the photoresist was 36 nm close to one tenth of λ_1. Furthermore, the narrow lines were spaced by 350 nm, which corresponds to the period of the λ_2 standing wave. We separately confirmed that the photoresist is not sensitive to the λ_2 photons. Those λ_1 peaks that coincide with the λ_2 peaks are suppressed beyond the photochromic layer. We confirmed this experimentally by recording lines at lower intensity ratios and examining their cross sections in the scanning electron microscope (fig. S6). In our current setup, in order to maintain high intensity in the λ_2 peaks, it was necessary to forgo spatial filtering of the λ_2 illumination. High-frequency noise therefore persisted in the λ_2 standing wave, causing line edge roughness as well as the line-width variation in the photoresist patterns. Nevertheless, these results clearly demonstrate the feasibility of deep subwavelength localization of light by using absorbance modulation.

Furthermore, these results also demonstrate the feasibility of patterning periodic lines far smaller than their spatial period. Because the absorbance of the AML is reversible, interspersed multiple exposures could pattern lines spaced apart by a distance far smaller than the far-field diffraction limit of the optical system. Although the current demonstration utilized one-dimensional standing waves, we anticipate straightforward extension to two-dimensional peaks and nodes, which can be generated with diffractive micro-optics (*24*, *25*). Furthermore, such nanoscale optical beams may also be useful for optical nanoscopy (*26*).

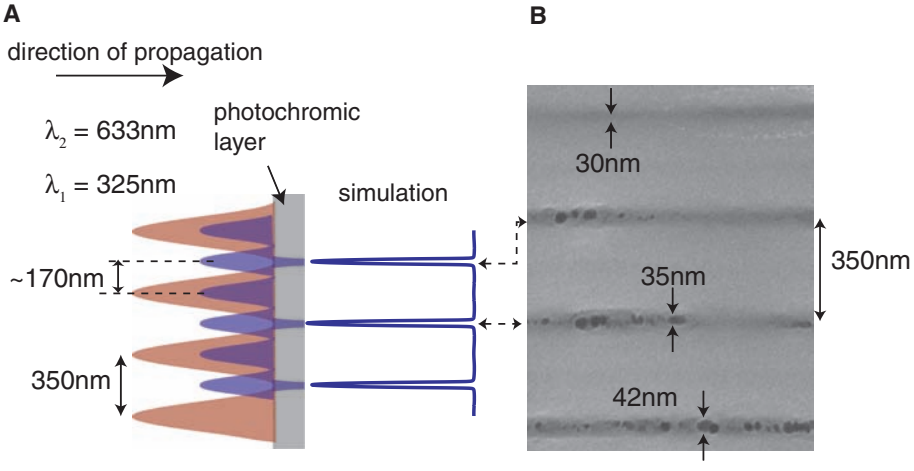

Fig. 4. Deep subwavelength patterning using absorbance modulation. (**A**) The photochromic layer is illuminated by two overlapping standing waves with periods of 350 nm (λ_2 = 633 nm) and 170 nm (λ_1 = 325 nm), respectively. Simulating the transmitted light at λ_1 supported narrow lines where the peaks of the λ_1 standing wave coincided with the nodes of the λ_2 standing wave. (**B**) Scanning electron micrograph of lines exposed in photoresist. Although the photoresist is underexposed, the lines represent a recording of the aerial image that is consistent with simulation.

References and Notes

1. E. Abbé, *Arch. Mikrosk. Anat. Entwichlungsmech.* **9**, 413 (1873).
2. K. Murooka, K. Hattori, O. Iizuka, *J. Vac. Sci. Technol. B* **21**, 2668 (2003).
3. R. F. W. Pease, *Microelectron. Eng.* **78**, 381 (2005).
4. E. A. Ash, G. Nichols, *Nature* **237**, 510 (1972).
5. E. Betzig, J. K. Trautman, T. D. Harris, J. S. Weiner, R. L. Kostelak, *Science* **251**, 1468 (1991).
6. L. Novotny, B. Hecht, D. Pohl, *Ultramicroscopy* **71**, 341 (1998).
7. H. G. Frey, F. Keilmann, A. Kriele, R. Guckenberger, *Appl. Phys. Lett.* **81**, 5030 (2002).
8. T. Ito *et al.*, *Appl. Phys. Lett.* **89**, 033113 (2006).
9. X. Yin, N. Fang, X. Zhanga, I. B. Martini, B. J. Schwartz, *Appl. Phys. Lett.* **81**, 3663 (2002).
10. A. Chovin, P. Garrigue, I. Manek-Hönninger, N. Sojic, *Nano Lett.* **4**, 1965 (2004).
11. E. Ozbay, *Science* **311**, 189 (2006).
12. N. Fang, H. Lee, C. Sun, X. Zhang, *Science* **308**, 534 (2005).
13. Z. Jacob, L. V. Alekseyev, E. Narimanov, *Opt. Exp.* **14**, 8247 (2006).
14. J. C. Crano, R. J. Guglielmetti, Eds., *Organic Photochromic and Thermochromic Compounds* (Plenum, New York, 1999).
15. R. Menon, H. I. Smith, *J. Opt. Soc. Am. A* **23**, 2290 (2006).
16. R. Menon, R. H.-Y. Tsai, S. W. Thomas, *Phys. Rev. Lett.* **98**, 043905 (2007).
17. H.-Y. Tsai, G. M. Wallraff, R. Menon, *Appl. Phys. Lett.* **91**, 094103 (2007).
18. Materials and methods are available as supporting material on *Science* Online.
19. Y. Yokoyama, *Chem. Rev.* **100**, 1717 (2000).
20. M. Irie, *Chem. Rev.* **100**, 1685 (2000).
21. P. J. Darcy, H. G. Heller, P. J. Strydom, J. Whittall, *J. Chem. Soc. Perkin Trans.* **1**, 202 (1981).
22. A. Taflove, S. C. Hagness, *Computational Electrodynamics: the Finite-Difference Time-Domain Method* (Artech House, Boston, 2000).
23. T. Ito *et al.*, *Appl. Phys. Lett.* **89**, 033113 (2006).
24. R. Menon, H.-Y. Tsai, P. Rogge, *J. Opt. Soc. Am. A.* **26**, 297 (2009).

25. H.-Y. Tsai, H. I. Smith, R. Menon, *Opt. Lett.* **33**, 2916 (2008).
26. S. W. Hell, *Nat. Biotechnol.* **21**, 1347 (2003).
27. We thank F. Stellacci and T. Swager for advice on synthesis of the photochromic molecules, H. Koh for the ellipsometric measurements, T. O'Reilly for assistance with the Lloyd's-mirror interferometer, and H. Smith for suggestions on the manuscript. T.L.A. was partially funded by a subcontract (6916866) from LumArray. H.-Y.T. was partially funded by an ignition grant from the MIT Deshpande Center for Technological Innovation. R.M. was partially funded by a Defense Advanced Research Projects Agency Small Business Innovation Research award (W31P4Q-05-C-R156). Three patents have been filed through MIT based on the work presented herein.

Supporting Online Material
www.sciencemag.org/cgi/content/full/1167704/DC1
Materials and Methods
SOM Text
Figs. S1 to S6
Table S1
References

27 October 2008; accepted 24 February 2009
Published online 9 April 2009;
10.1126/science.1167704
Include this information when citing this paper.

Size and Shape of Saturn's Moon Titan

Howard A. Zebker,[1]* Bryan Stiles,[2] Scott Hensley,[2] Ralph Lorenz,[3] Randolph L. Kirk,[4] Jonathan Lunine[5]

Cassini observations show that Saturn's moon Titan is slightly oblate. A fourth-order spherical harmonic expansion yields north polar, south polar, and mean equatorial radii of 2574.32 ± 0.05 kilometers (km), 2574.36 ± 0.03 km, and 2574.91 ± 0.11 km, respectively; its mean radius is 2574.73 ± 0.09 km. Titan's shape approximates a hydrostatic, synchronously rotating triaxial ellipsoid but is best fit by such a body orbiting closer to Saturn than Titan presently does. Titan's lack of high relief implies that most—but not all—of the surface features observed with the Cassini imaging subsystem and synthetic aperture radar are uncorrelated with topography and elevation. Titan's depressed polar radii suggest that a constant geopotential hydrocarbon table could explain the confinement of the hydrocarbon lakes to high latitudes.

The Cassini spacecraft has been orbiting Saturn for 4 years, observing Titan periodically. When close to Titan, it can return surface elevation data from a nadir-pointing radar altimeter (*1*) and a multiple-beam synthetic aperture radar (SAR) imaging system (*2*, *3*). We have used these radar instrument modes to estimate the surface elevation by measuring the time delay of the altimeter echoes and the precise radar look angle to points on the surface by processing the multibeam SAR images with monopulse methods (Fig. 1) (*4*).

In the radar altimeter mode, the instrument transmits energy nearly vertically to the planetary surface below and records the received echo as a function of time; we corrected the data for biases due to mis-pointing errors (*1*). The Cassini altimetry data products record both the leading-edge location and the average delay of the return echo, but we used the mean return in order to estimate the mean surface height.

The SAR imaging system on Cassini comprises five parallel beams that produce a much wider ground swath than would have been possible with the use of a single beam. Each beam is time-shared in order to maintain a contiguous swath on the ground (*5*, *6*), so we sacrificed along-track resolution, averaging, and signal-to-noise ratio for the sake of the increased swath width. This is the burst-mode or ScanSAR imaging configuration, and it returns five overlapping observation swaths from the surface. The differencing of power images from the overlapped sections of adjacent beams forms an amplitude monopulse system to measure the precise angle to a given point on the ground (*4*, *7*), which, combined with knowledge of the spacecraft imaging geometry, yields a surface height measurement. Hence, under this analysis, most of the SAR imaging passes also provide estimates of the elevation at the beam overlap regions. Although this method is more elaborate than altimetry, it provides wider coverage because SAR imaging is used more often. We used all possible beam overlaps containing pixels sufficiently bright that the intensity differences were meaningful. The effective footprint of each measurement is roughly the SAR resolution (0.5 km) in the range direction and 10 km in the along-track direction.

These techniques show that the poles of Titan lie at lower elevations than the equator and that the topography also varies longitudinally (Fig. 1). Measurements in the polar regions yield elevations of about –600 to –700 m, referenced to a 2575-km-radius sphere, whereas Titan's

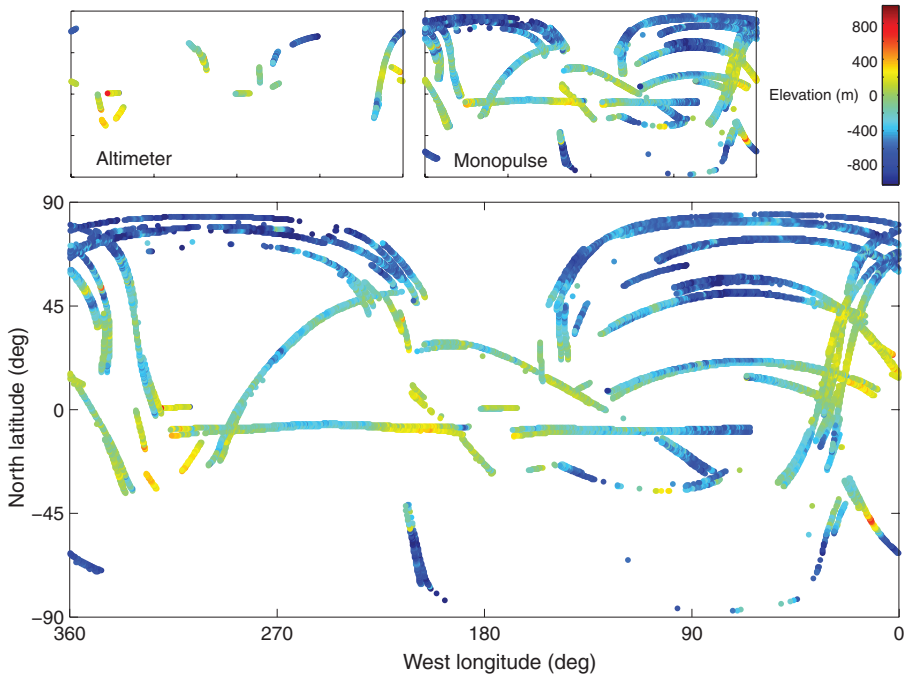

Fig. 1. Titan elevations observed with altimeter and SAR monopulse radar modes, cylindrical projection, displayed as deviation from an ideal 2575 km sphere located at Titan's barycenter. Locations on the figure give the latitude and west longitude of each measurement. Far more coverage is available from the monopulse mode than from altimetry, but these data are not as accurate as the altimeter measurements.

[1]Departments of Geophysics and Electrical Engineering, Stanford University, Stanford, CA 94305, USA. [2]Jet Propulsion Laboratory (JPL), California Institute of Technology, 4800 Oak Grove Drive, Pasadena, CA 91109, USA. [3]Applied Physics Laboratory, Johns Hopkins University, 11100 Johns Hopkins Road, Laurel, MD 20723, USA. [4]U.S. Geological Survey, 2255 North Gemini Drive, Flagstaff, AZ 86001, USA. [5]Departments of Planetary Science and Physics, University of Arizona, Tucson, AZ 85721, USA.

*To whom correspondence should be addressed. E-mail: zebker@stanford.edu